

Alma Mater Studiorum Università di Bologna  
Archivio istituzionale della ricerca

Hydrogen Desorption below 150 °c in MgH<sub>2</sub>-TiH<sub>2</sub> Composite Nanoparticles: Equilibrium and Kinetic Properties

This is the final peer-reviewed author's accepted manuscript (postprint) of the following publication:

*Published Version:*

Patelli, N., Calizzi, M., Migliori, A., Morandi, V., Pasquini, L. (2017). Hydrogen Desorption below 150 °c in MgH<sub>2</sub>-TiH<sub>2</sub> Composite Nanoparticles: Equilibrium and Kinetic Properties. JOURNAL OF PHYSICAL CHEMISTRY. C, 121(21), 11166-11177 [10.1021/acs.jpcc.7b03169].

*Availability:*

This version is available at: <https://hdl.handle.net/11585/604782> since: 2017-07-20

*Published:*

DOI: <http://doi.org/10.1021/acs.jpcc.7b03169>

*Terms of use:*

Some rights reserved. The terms and conditions for the reuse of this version of the manuscript are specified in the publishing policy. For all terms of use and more information see the publisher's website.

This item was downloaded from IRIS Università di Bologna (<https://cris.unibo.it/>).  
When citing, please refer to the published version.

(Article begins on next page)

This is the final peer-reviewed accepted manuscript of:

Nicola Patelli, Marco Calizzi, Andrea Migliori, Vittorio Morandi, and Luca Pasquini, Hydrogen Desorption Below 150 °C in MgH<sub>2</sub>–TiH<sub>2</sub> Composite Nanoparticles: Equilibrium and Kinetic Properties in *Journal of Physical Chemistry C*, 2017, 121, 21, 11166–11177.

The final published version is available online at:  
<https://doi.org/10.1021/acs.jpcc.7b03169>

#### Rights / License:

The terms and conditions for the reuse of this version of the manuscript are specified in the publishing policy. For all terms of use and more information see the publisher's website.

This item was downloaded from IRIS Università di Bologna (<https://cris.unibo.it/>)

**When citing, please refer to the published version.**

# Hydrogen desorption below 150 °C in MgH<sub>2</sub>-TiH<sub>2</sub> composite nanoparticles: equilibrium and kinetic properties

Nicola Patelli,<sup>1</sup> Marco Calizzi,<sup>1,a</sup> Andrea Migliori,<sup>2</sup> Vittorio Morandi,<sup>2</sup> Luca Pasquini<sup>1</sup>

1- Department of Physics and Astronomy, University of Bologna, Italy

2 – National Research Council, Institute for Microelectronics and Microsystems,  
Unit of Bologna, Italy

a: corresponding author

**Abstract:** Reversible hydrogen sorption coupled with the MgH<sub>2</sub>↔Mg phase transformation was achieved in the remarkably low 340 - 425 K temperature range using MgH<sub>2</sub>-TiH<sub>2</sub> composite nanoparticles obtained by reactive gas-phase condensation of Mg-Ti vapours under He/H<sub>2</sub> atmosphere. The equilibrium pressures determined by *in situ* measurements at low temperature were slightly above those predicted using enthalpy  $\Delta H$  and entropy  $\Delta S$  of bulk magnesium. A single van 't Hoff fit over a range extended up to 550 K yields the thermodynamic parameters  $\Delta H = 68.1 \pm 0.9$  kJ/molH<sub>2</sub> and  $\Delta S = 119 \pm 2$  J/K·molH<sub>2</sub> for hydride decomposition. A desorption rate of 0.18 wt% H<sub>2</sub>/min was measured at T=423 K and p(H<sub>2</sub>)≈ 1 mbar, i.e. close to equilibrium, without using a Pd catalysts. The nanoparticles displayed a small absorption-desorption pressure hysteresis even at low temperatures. We critically discuss the influence exerted by nanostructural features such as interface free energy, elastic clamping, and phase mixing at the single nanoparticle level on equilibrium and kinetic properties of hydrogen sorption.

## INTRODUCTION

The equilibrium and transport properties of materials can be modified and -to some extent- tailored when the size of their building domains become similar to, or smaller than, a characteristic length scale, such as the electron / phonon mean free path, the width of magnetic domain walls, the correlation length of thermal fluctuations. Moreover, many property changes arise from the large fraction of atoms located at under-coordinated or partly disordered surface / interface sites in nanomaterials, e.g. enhanced atomic and ionic transport by diffusion, reduced melting temperature, and higher vapour pressure. The rich diversity of phenomena associated with nanoscaling has pervaded almost all areas of materials science. Along this mainstream, the desire to understand and control the interaction of hydrogen with nanoscale materials has stimulated many research efforts, bringing significant achievements and at the same time leaving many intriguing open questions [1,2]. Quite schematically, three fundamental processes describe the hydrogen-metal interaction. The first is dissociation/recombination of the hydrogen molecule into/from atomic hydrogen at the surface, with barrier height  $E_{diss}$ . Dissociation is the starting step of the absorption sequence, while recombination is the last occurring in desorption. Both may involve physisorption of molecular hydrogen, with an enthalpy small in absolute value (typically 5 to 10 kJ/mol H<sub>2</sub>). The second process is diffusion of atomic hydrogen in the solid, with an activation energy  $E_{diff}$  that is generally different in the metal and in the hydride. The associated transport of atomic hydrogen from/toward the surface is often a rate limiting step in bulk materials. This process comprises crossing of a near surface layer with specific activation energy. The third process is formation/decomposition of the hydride, with enthalpy  $\Delta H$  and entropy  $\Delta S$ . The formation of the hydride, which for non-interstitial hydrides modifies the lattice structure, is preceded by dissolution of hydrogen within the metal lattice, sometimes with very small solubility limits.

The interplay of dissociation/recombination and diffusion determines the kinetics of the metal-hydride reversible transformation and of the associated hydrogen storage and release [3]. However, the parameters  $E_{diss}$  and  $E_{diff}$ , relevant as they are to sorption rates, have no direct relations to the equilibrium pressure and

temperature of hydrogen sorption, which depend only on  $\Delta H$  and  $\Delta S$ . The enthalpy of hydride formation varies significantly across the periodic table: it is positive for elements that form unstable hydrides such as Be, Fe, and Cu to name a few, and reaches large negative values in highly stable hydrides like  $\text{LaH}_2$  (-208 kJ / mol  $\text{H}_2$ ) [4]. Differently, the entropy  $\Delta S$  varies moderately among various materials, since it mainly comes from consuming or producing hydrogen gas. Therefore, the absolute value of  $\Delta S$  is close to the standard entropy of a perfect gas, i.e.  $\approx 130$  J/K mol $\text{H}_2$ . The temperature  $T_{eq}^{1\text{ bar}}$ , at which the metal and the hydride are in equilibrium with each other and with gaseous hydrogen at a pressure  $p(\text{H}_2)=1$  bar, is given by  $T_{eq}^{1\text{ bar}} = \Delta H / \Delta S$ . The equilibrium conditions in a nanomaterial can therefore be changed compared to its bulk counterpart if it is possible to modify  $\Delta H$  or  $\Delta S$ , or both. The possibility of tailoring  $\Delta H$  has stimulated more research, because  $\Delta S$  is expected to lean on the aforementioned perfect gas entropy. Nevertheless, it is clear from the above that a  $\Delta H$  change would be ineffective on  $T_{eq}^{1\text{ bar}}$  when paralleled by a  $\Delta S$  change of the same relative amount in the same direction.

In many applications, the goal is to lower the temperature of hydrogen release, i.e. to destabilize the hydride. For instance, the holy grail of room temperature hydrogen storage is a lightweight hydride with formation enthalpy of about -40 kJ/mol  $\text{H}_2$ . Therefore, starting from a too stable bulk hydride, one seeks nanostructural features that render  $\Delta H$  less negative. A possible tool is the interface/surface free energy: if it is larger in the hydride than in the metal, the net effect is a positive thermodynamical bias that destabilizes the hydride [5–7]. Another suggested approach is elastic strain engineering, in which boundary constraints are applied in order to tune  $\Delta H$  by means of compressive strains [8,9].

Magnesium and its hydride have been widely investigated both theoretically and experimentally, mainly thanks to high gravimetric/volumetric hydrogen capacity and favourable cost [10,11]. Furthermore,  $\text{MgH}_2$  has been employed in reactive hydride composites, particularly in conjunction with  $\text{LiBH}_4$  [12]. The main drawbacks of Mg for reversible hydrogen storage close to ambient conditions are the high stability (with  $\Delta H$  about -74 kJ/ mol $\text{H}_2$ ) and the sluggish sorption kinetics. Even if many studies suggested that  $\Delta H$  and  $\Delta S$  of Mg-based nanomaterials remain very close to their bulk values [13–16], some authors reported a significant  $\Delta H$  reduction (in absolute value) [17–19]. Unfortunately, no concomitant decrease of  $T_{eq}^{1\text{ bar}}$  was observed. The existence of an enthalpy-entropy compensation effect was proposed, although the subject is knowingly quite controversial in the literature [20]. To the best of our knowledge, a destabilizing bias in pure  $\text{MgH}_2$  was only achieved in carefully interface-engineered ultra-thin films and matrix-embedded nanoclusters [7,21], and was measured only at low temperature where the nanostructure is stable.

On the other hand, a remarkable progress was made in improving the Mg hydrogen sorption kinetics by nanostructuring (see [11] and refs therein). Hydrogen absorption by Mg was observed down to room temperature by using suitable catalyst [11,13]. However, reversible desorption with reasonable kinetics invariably required  $T > 150^\circ\text{C}$ , the only exception being Mg thin films capped by a Pd catalyst layer. Considering that Pd is extremely expensive and thin films are not compatible with upscaling, the applicability of these systems in low-temperature reversible hydrogen stores is clearly strongly limited. Recently, several groups have studied  $\text{TiH}_2$  as alternative kinetic facilitator [13,14,22–26]. Since Mg and Ti are immiscible, the required dispersion of  $\text{TiH}_2$  in Mg/ $\text{MgH}_2$  was principally achieved by ball milling, multilayer deposition or wet chemistry.

In this work, we developed a new strategy that permitted to grow small Mg-Ti-H nanoparticles (NPs), in which  $\text{TiH}_2$  and Mg/ $\text{MgH}_2$  coexist at the single NP level, despite the bulk immiscibility of Mg and Ti. Hydrogenated NPs were directly obtained by gas phase condensation in a  $\text{H}_2$ -enriched He atmosphere. In this way, a unique novel nanostructure was realized, in which the high  $\text{MgH}_2/\text{TiH}_2$  interface area and the small domain size concur in promoting outstanding kinetic properties. This permitted to achieve fast kinetics even at low temperature and thus to determine the equilibrium pressures of both absorption and desorption in a previously inaccessible temperature range down to 340 K. The obtained  $\Delta H$  and  $\Delta S$  values, which display only small departure from those of bulk Mg, are discussed within the frame of a thermodynamic model and

critically compared to recent literature results on Mg-based and Mg-Ti-based nanomaterials. Besides showing fast kinetics, the Mg-Ti-H NPs exhibited a small pressure hysteresis also in the low temperature regime. In summary, our synthesis technique is compatible with scale up and opens a new temperature/pressure window for reversible hydrogen storage in Mg.

## EXPERIMENTAL METHODS

Mg-Ti-H nanoparticles (NPs) were synthesized by Reactive Gas Condensation (RGC) using Mg ingots (Alpha Aesar 99.95% purity) and Ti powder (Alpha Aesar 99.9%, 150 mesh) as precursor metals. An ultra-high-vacuum (UHV) chamber equipped with two tungsten boats as thermal sources was preliminarily evacuated to  $2 \cdot 10^{-7}$  mbar and subsequently filled with an equimolar He / H<sub>2</sub> mixture (99.9999% purity) up to a final pressure of 2.6 mbar. The heating currents applied to the Mg and Ti vapour sources, which were positioned about 1 cm apart in order to favour vapour mixing, were initially tuned to achieve the desired Ti/Mg ratio. The individual evaporation rates were also monitored by a quartz crystal microbalance to improve composition control. NPs nucleation occurs from the gas phase because the metal vapours quickly become supersaturated via collisions and thermalization with the ambient He / H<sub>2</sub> gas. The NPs were continuously collected by thermophoresis onto a rotating stainless steel cylinder filled with liquid nitrogen. Finally, the NPs were scraped off and transferred under high vacuum into a secondary volume-calibrated UHV chamber equipped with a sample heating stage. NPs batches with average  $X_{Ti} \equiv Ti/(Mg+Ti)$  atomic ratio of 6, 15, 30 and 60 at.% were prepared. From here on, we will call the corresponding samples Mg- $X_{Ti}$  Ti.

Hydrogen sorption properties were studied under isothermal conditions using two different set-ups depending on the explored temperature range. Measurements in the 340 K < T < 425 K, the main novelty of this paper, were carried out in the secondary UHV chamber, where the combination of a thermal conductivity vacuum sensor with a capacitive pressure sensor covered the  $10^{-2} - 10^3$  mbar range. For measurements in the 430 K < T < 550 K range, we employed a homemade Sievert's apparatus.

The plateau pressures for hydrogen absorption ( $P_{abs}$ ) and desorption ( $P_{des}$ ) were determined following a measurement sequence, schematized in Figure 1, specifically devised for dealing with low equilibrium pressures (down to about 0.1 mbar for T≈340 K). We actually measured the pressures that in a full Pressure-Composition-Isotherm (PCI) would be the knees where desorption and absorption plateaus start. More details about the measurements strategy are given in the Supplementary Information (SI) file. The equilibrium pressure at each temperature was calculated as the geometric average  $P_{eq} = \sqrt{P_{abs} \cdot P_{des}}$ .

The crystalline phases in the samples were characterized by a PANalytical X'celerator diffractometer employing Cu  $K_{\alpha}$  radiation. X-Ray Diffraction (XRD) patterns were analyzed with the MAUD Rietveld-refinement software to determine the lattice parameters, crystallite size and relative phase abundance.

The overall  $X_{Ti}$  was determined using a Leica Cambridge Stereoscan 360 Scanning Electron Microscope equipped with an Oxford Instruments X-ray detector for energy dispersive X-ray microanalysis (EDX).

In order to gain insight on the element distribution at the single NP level, we performed a morphological and elemental analysis with a FEI Tecnai F20 ST Transmission Electron Microscope operated in scanning mode (STEM) at 200 keV. The use of an EDX detector in STEM mode allowed the profiling of Mg and Ti elemental distribution with a spatial resolution of about 2 nm. For STEM analysis, the NPs were dispersed in ethanol and the sonicated suspension was drop-casted on a holey carbon support grid.

For all analysis and characterization measurements outside the synthesis system, the NPs were extracted from the secondary UHV chamber inside a sealed glass container under a slight Ar overpressure. Before the extraction, the NPs were subjected to hydrogen absorption for 2 hours at T=400 K and p(H<sub>2</sub>) = 130 mbar. In

the following, the NPs treated in this way and just extracted from the UHV chamber will be named *as-prepared NPs*, to distinguish them from those treated at higher temperature in the Sievert apparatus. The NPs transfer into the appropriate sample holders was done inside an Ar-filled glove bag.

## RESULTS

### Crystalline phases, microstructure and morphology of as-prepared NPs

Figure 2 displays the XRD patterns of the as-prepared NPs. The corresponding quantitative Rietveld analyses are summarized in Table 1.  $\text{MgH}_2$  occurs in two phases: rutile-type tetragonal  $\beta\text{-MgH}_2$  and orthorhombic  $\gamma\text{-MgH}_2$ , a polymorph that is stable at high pressure and is usually found in ball-milled  $\text{MgH}_2$  [14]. The  $\beta\text{-MgH}_2$  crystallite size  $d_{\text{MgH}_2}$  decreases with increasing  $X_{\text{Ti}}$ , as already observed for Mg-Ti NPs synthesized under inert He atmosphere [27]. The lattice parameters of the  $\beta\text{-MgH}_2$  phase (Table 1) in the NPs are very close to the bulk values ( $a=4.5185$  Å and  $c=3.0220$  Å, this work, or  $a=4.5180$  Å and  $c=3.0211$  Å [28]), the discrepancy being lower than 0.1% for all samples. Figure S1 of the Supplementary Information (SI) displays the relative variation of the  $\beta\text{-MgH}_2$  unit cell volume in the Mg-Ti-H NPs with respect to bulk  $\beta\text{-MgH}_2$ , measured as a function of  $X_{\text{Ti}}$ . If Ti solubility in  $\text{MgH}_2$  occurred, one would expect a shrinkage of the unit cell by about 0.3% per at.% Ti [29]. Figure S1 shows a very small volume expansion in the 0.05 to 0.2 % range, demonstrating that, if any solubility of Ti in  $\beta\text{-MgH}_2$  occurs within the NPs, it is below 0.2 at.% for sample Mg-6Ti and remains below 1 at.% even at the higher Ti content ( $X_{\text{Ti}}= 30, 60$  at.%).

The  $\beta\text{-MgH}_2$  to  $\gamma\text{-MgH}_2$  weight ratio diminishes slightly from ~5.4 to ~4.3 with increasing  $X_{\text{Ti}}$  from 6 to 30 at.%. The  $\gamma\text{-MgH}_2$  reflections are not observable in the XRD pattern of sample Mg-60Ti, but this does not rule out its presence. In fact, the detection and the quantitative analysis of minority phases in these NPs are rather difficult and prone to large relative errors, if not impossible, because of the severe line broadening due to the small size of coherently diffracting domains.

The identification of the  $\text{TiH}_2$  crystalline phase in the NPs is less straightforward.  $\text{TiH}_2$  is known to exhibit a transition from a fluorite cubic structure ( $\delta\text{-TiH}_2$ , space group  $Fm\bar{3}m$ ) to a tetragonal structure ( $\varepsilon\text{-TiH}_2$ , space group  $I4/mmm$ ) at about 17 °C [30] on cooling. The same transition is observed with increasing pressure above 2.2 GPa. The  $\varepsilon$ -phase was also detected as majority  $\text{TiH}_2$  phase in  $\text{MgH}_2\text{-TiH}_2$  ball-milled nanocomposites on a wide composition range [14]. Following the cubic-tetragonal transition, the (200), (220) and (311) reflections of the cubic structure split in two tetragonal reflections. In our XRD patterns, the line broadening makes it difficult to distinguish between the two phases. Nevertheless, the Rietveld refinement of Mg-30Ti and Mg-60Ti reveals that the tetragonal  $\varepsilon\text{-TiH}_2$  phase dominates. The better fit quality obtained with  $\varepsilon\text{-TiH}_2$  is clearly shown for sample Mg-30Ti in Figure S2 (SI) and is corroborated by a significant decrease of  $R_{\text{wp}}$  values. In the samples Mg-6Ti and Mg-15Ti, the low Ti content does not allow to identify unambiguously the  $\text{TiH}_2$  phase because the fit quality does not change significantly and the reflections at high angles are very weak. We report in Table 1 the results that are obtained assuming the presence of the tetragonal phase. The  $\text{TiH}_2$  crystallite size  $d_{\text{TiH}_2}$  decreases with increasing Mg content, reaching an extremely low value of about 2.5 nm in sample Mg-6Ti. The lattice parameters could be determined reliably only for samples Mg-30Ti and Mg-60Ti with a higher Ti content: the relative variation of the unit cell volume with respect to ball-milled  $\varepsilon\text{-TiH}_2$  powders [14] is displayed in Figure S1, showing a volume expansion of about 1.4 %. Using Vegard's law and literature data for  $\text{MgH}_2$  and  $\text{TiH}_2$  cell volumes [14,29], we can attribute this result to a Mg solubility in  $\text{TiH}_2$  of about 5 at.%. This conclusion is also supported by Figure S3 (SI), which depicts the  $\text{Mg}/(\text{Mg}+\text{Ti})$  ratio obtained from the Rietveld phase abundances. The clear Mg underestimation

compared to EDX results may well be due to a certain degree of Mg solubility in TiH<sub>2</sub>, which the Rietveld model does not account for.

The other phase observed in relevant amount is MgO, which exhibits broad lines indicating a very small crystallite size of 4-5 nm for all samples. Its fraction, which never exceeds 10 wt%, is remarkably low compared to previous reports on Mg-based NPs of similar size [27,19]. The H<sub>2</sub>-enriched synthesis atmosphere likely plays a role here. In fact, once NPs are cooled below about 390 K by collision with the gas molecules, the thermodynamic conditions for MgH<sub>2</sub> formation become satisfied at the applied partial pressure p(H<sub>2</sub>)=1.3 mbar. Figure S4 indeed shows that the NPs contain a mixture of Mg and MgH<sub>2</sub> just after the synthesis, before the in situ hydrogen absorption treatment in the secondary UHV chamber. The hydride likely develops at the NPs' surface and may thus act as a protecting coating against oxidation by residual oxygen and/or water impurities. The fraction of oxidized Mg atoms calculated from the Rietveld analysis exhibits a positive correlation with  $X_{Ti}$ , increasing from about 5% in Mg-6Ti to 15% in Mg-60 Ti.

It is worth noticing that the as-prepared NPs are relatively stable against oxidation even under ambient conditions. In fact, the XRD patterns reported in Figure 2 were collected under air in a typical time of about 1 hour. No significant changes in the patterns were observed by immediately repeating the measurements.

Finally, small residues of metallic Mg are detected (1-3 wt%), while neither metallic Ti nor Ti oxides are observed, confirming that hydride formation is almost completed in the as-prepared NPs.

**Table 1:** Weight fraction of the crystalline phases in as-prepared NPs (upper part) as a function of  $X_{Ti}$ , determined by Rietveld refinement of XRD profiles. For the phases  $\beta$ -MgH<sub>2</sub> and  $\epsilon$ -TiH<sub>2</sub>, the crystallite size  $d$  and lattice parameters are also reported. Rietveld agreement factors  $R_{wp}$  and  $R_{exp}$  are given. The numbers in parenthesis represent the standard deviations referred to the last digit. Where no error is given, the parameter was fixed to ensure fit stability due to the low phase amount and/or very small crystallite size. The lower part of the table reports the same data for the NPs after hydrogen sorption cycles at T>430 K.

$X_{Ti}$	$\beta$ -MgH <sub>2</sub>				$\epsilon$ -TiH <sub>2</sub>				MgO	$\gamma$ -MgH <sub>2</sub>	Mg	$R_{wp}$	$R_{exp}$
at.%	wt%	$d_{MgH_2}$ (nm)	$a$ (Å)	$c$ (Å)	wt%	$d_{TiH_2}$ (nm)	$a$ (Å)	$c$ (Å)	wt%	wt%	wt%	(%)	(%)
<b>as-prepared NPs</b>													
6(1)	65(5)	20(2)	4.5190(2)	3.0229(3)	16(3)	2.5(5)	3.1871	4.381	6(2)	12(1)	1	5.1	1.3
15(2)	53(5)	18(2)	4.5200(6)	3.0224(7)	26(3)	6(1)	3.1871	4.381	10(1)	10(1)	1	6.7	2.0
30(3)	34(3)	15(1)	4.5224(4)	3.0227(5)	49(5)	7(1)	3.1871(6)	4.381(2)	9(1)	8 (1)	2(1)	4.0	1.9
60(5)	8(1)	13(1)	4.5205	3.0267	86(7)	9(1)	3.196(1)	4.360(2)	3(1)	0	3(1)	5.7	2.2
<b>after hydrogen sorption cycles at T&gt; 430 K</b>													
6(1)	78(5)	80(8)	4.5193(2)	3.0225(1)	13(2)	4	3.1831	4.386	9(1)	0	0	5.5	2.8
30(3)	36(4)	25(3)	4.5207(4)	3.0242(3)	55(5)	7(1)	3.1831(7)	4.386(2)	9(1)	0	1	5.1	2.1
60(5)	7(2)	14	4.529(2)	3.0267	85(7)	8(1)	3.192(1)	4.381(2)	8(2)	0	0	6.4	2.8

Figure 3 displays High Angle Annular Dark Field (HAADF)-STEM images of as prepared NPs Mg-6Ti (a, c) and Mg-30Ti (b, d). These results are representative of a large number of investigations on similar NPs. The average NPs diameter extracted from a series of HAADF-STEM images (Figure S5) coincides within the uncertainties with  $d_{MgH_2}$ , thus suggesting a one-to-one correspondence between NPs and  $\beta$ -MgH<sub>2</sub> crystallites. The contrast  $C$  in incoherent HAADF images is proportional to  $Z^{1.7} \cdot t$ , where  $Z$  is the atomic number and  $t$  is the specimen thickness, consequently the brighter particles, for the same size can be

ascribed to a Ti-rich phase in the NPs, i.e. to  $\text{TiH}_2$  based on XRD analysis. Furthermore, STEM-EDX line-scans of Mg and Ti elements (Fig. 3 e, f) detect the X-ray fluorescence of both elements at almost every step inside the NPs. The count fluctuations represent local compositional changes and/or thickness variations. Since  $\text{MgH}_2$  and  $\text{TiH}_2$  are electron-beam sensitive [31] and tend to decompose during the observations, it was not possible to characterize the phase distribution by electron diffraction. In summary, the following picture emerges from combined XRD and STEM analyses: each NP is a nanocomposite, where ultra-fine  $\text{TiH}_2$  crystallites are dispersed within an  $\text{MgH}_2$  matrix constituted by a single crystalline grain. The  $\text{TiH}_2$  crystallites actually contain some dissolved Mg, whereas no significant solubility of Ti in  $\text{MgH}_2$  occurs.

## Hydrogen sorption and thermal stability

Hydrogen sorption properties were initially characterized at low temperature ( $340 \text{ K} < T < 425 \text{ K}$ ) in the secondary UHV chamber of the synthesis apparatus. We focussed primarily on hydrogen sorption close to the equilibrium, with the aim to determine  $P_{abs}$  and  $P_{des}$  as described in the experimental methods. Figure 4 illustrates the typical amount and time scale of pressure variations for sample Mg-15Ti at 375 K. The desorption and absorption curves correspond to steps II and V, respectively, of the measurement sequence sketched in Figure 1. The decreasing slope of  $p(\text{H}_2)$  vs time does not indicate that the metal $\leftrightarrow$ hydride transformation is complete, but that its driving force vanishes as the  $P_{eq}$  is approached. Indeed, after restoring the initial values, the pressure restarts to change, approaching again the equilibrium. The repetition of several desorption steps permits to construct a full Pressure-Composition Isotherm (PCI), as represented by the desorption branch in Figure 5. Similarly, a series of absorption steps builds up the PCI absorption branch (Figure 5). The low equilibrium pressures in this temperature range, together with the high storage capacity of the material, call for many lengthy measurements steps to complete a PCI branch. For instance, the PCI in Figure 5 took about two weeks. For this reason, the equilibrium properties were mainly determined by the procedure sketched in Figure 1 rather than through full PCIs. The main motivation behind this choice is to limit as much as possible the amount of coarsening and microstructure evolution, which occurs during the measurement themselves, as we will discuss later on.

Qualitatively similar results were obtained on NPs with  $X_{\text{Ti}}=6$  and 30 at.%. As an example, Figure S6 displays the hydrogen sorption curves recorded at 355 K on sample Mg-6Ti. The only exception is sample Mg-60Ti that exhibits pressure variations an order of magnitude smaller on very long times. These features impeded a reliable determination of its hydrogen sorption properties, which will not be presented here. The main causes for this failure are the significantly lower amount of Mg and the higher degree of Mg oxidation, as discussed in the previous section.

All  $P_{eq}$  values measured on Mg-Ti-H NPs with  $X_{\text{Ti}}$  in the 6-30 at.% range are collected in a single van 't Hoff plot in Figure 6. The data fall reasonably well on a single straight line whose slope and intercept yield the enthalpy and entropy of hydride formation/decomposition, according to the van 't Hoff equation:

$$\ln\left(\frac{P_{eq}}{P_0}\right) = \frac{\Delta G}{RT} = \frac{\Delta H}{RT} - \frac{\Delta S}{R} \quad (1)$$

Where  $\Delta G$ ,  $\Delta H$  and  $\Delta S$  are the reaction's Gibbs free energy, enthalpy, and entropy at pressure  $P_0$ , and  $R$  is the gas constant. The results displayed in Figure 6:  $\Delta H=68.1\pm0.9 \text{ kJ/molH}_2$  and  $\Delta S=119\pm2 \text{ J/K}\cdot\text{molH}_2$ , are both lower than literature values obtained for bulk  $\text{MgH}_2$  at higher temperature:  $\Delta H_{bulk}=74.06\pm0.42 \text{ kJ/molH}_2$  and  $\Delta S_{bulk}=133.4\pm0.7 \text{ J/K}\cdot\text{molH}_2$  [15].

Another interesting parameter to address is the  $P_{abs}/P_{des}$  ratio, which quantifies the pressure hysteresis. In Figure 7, NPs are confronted to a Mg/Ti/Pd thin film (50 nm Mg) [7] and to Mg/Ti/Pd three-layer nanodots



(NDs) of different sizes [32]. The NPs clearly exhibit a much lower pressure hysteresis compared to these clamped systems.

Figure 8 demonstrates remarkably fast hydrogen sorption kinetics also in the low temperature range. The hydrogen absorption rate is 3.6 wt% H<sub>2</sub>/min at 423 K for an initial pressure about ten times larger than  $P_{abs}$ . At the same temperature, the hydrogen desorption rate is 0.18 wt% H<sub>2</sub>/min for  $0 < p(\text{H}_2) < 1$  mbar and then decreases rapidly because  $P_{des} \approx 3.1$  mbar is rapidly approached.

The Mg-Ti-H NPs exhibit a certain degree of microstructure evolution during hydrogen sorption cycling, which strongly depends on the time/temperature history. XRD patterns recorded after hydrogen sorption cycles are presented in Figure S7 and the Rietveld analyses are summarized in Table 1. The most evident changes are the disappearance of the metastable  $\gamma$ -MgH<sub>2</sub> phase in favour of  $\beta$ -MgH<sub>2</sub> and the coarsening of  $d_{\text{MgH}_2}$ . The lattice parameters of the  $\beta$ -MgH<sub>2</sub> and  $\epsilon$ -TiH<sub>2</sub> phases exhibit small relative changes below 0.1 % compared to as-prepared NPs. The MgO fraction remains approximately constant below 10 wt% for all samples. STEM investigations provide more detailed and local information on the microstructure evolution and highlight the dramatic influence of the maximum temperature experienced by the NPs. Figure 9 illustrates different situations that arise in a sample subjected to cycling at  $T < 425$  K. On one side, local coarsening phenomena are observed, which lead to the formation of larger NPs (about 100 nm size) containing Ti-free zones (Fig. 9 a,c). On the other, most NPs maintain the initial morphology and elemental distribution (Fig. 9 b,d), showing good thermal stability in this temperature range on a time window of approximately one month. At higher temperatures, coarsening phenomena and spectacular morphological changes become dominant. Figure S8 highlights two typical features: i) large Mg NPs, several hundreds of nm in size, where Ti is not uniformly distributed but concentrated in localized spots (Fig. S8 a,c), and ii) small NPs internally depleted from Mg, resulting in a nearly hollow morphology (Fig. S8 b,d). Formation of hollows was already observed after high temperature hydrogen cycling in larger Mg NPs and was explained by Mg diffusion and sublimation [33]. Only few NPs with size and morphology similar to as-prepared state can be detected after cycling in this temperature range.

## DISCUSSION

The possibility to tailor the equilibrium and kinetic properties of hydrogen sorption through nanosizing and nanoscale dispersion of different phases has driven many research efforts [1]. Figure 10 gathers several van 't Hoff plots selected from literature data on Mg and Mg-Ti nanomaterials. Quite remarkably, the equilibrium pressures measured at (or extrapolated to) 573 K vary in a narrow range from  $\sim 1$  bar to  $\sim 2.5$  bar, thus showing a relatively small spread around the bulk Mg value of  $\sim 1.8$  bar. This means that for any application where hydrogen release close to ambient pressure is needed, such as feeding a fuel cell, all systems collected in Figure 10 are very similar: they require a working temperature close to 550 K. Therefore, it is quite surprising that the corresponding  $\Delta H$  values, listed in Figure 10's legend, are often well below  $\Delta H_{bulk}$ . In fact, a  $\Delta G$  decrease (in absolute value) by 10 kJ/molH<sub>2</sub>, according to Eq. (1), should raise  $P_{eq}$  by a factor of  $\sim 8$  at 573 K. Invariantly, when  $\Delta H$  values significantly lower than  $\Delta H_{bulk}$  were reported,  $\Delta S$  was also lower than  $\Delta S_{bulk}$ , resulting in tiny  $P_{eq}$  changes.

Let us therefore examine the key ingredients that may lead to measurable equilibrium changes in nanomaterials. They may be grouped into four categories: 1) modification of the reaction by inclusion of new phases as reactants and products [34,35]; 2) compositional modifications by doping/alloying [36,37]; 3) contribution of interfaces/surfaces to the reaction's free energy [7,5,6], and 4) elastic confinement effects [8,9,38,39]. Clearly, items 1)-2) also apply to all materials classes, whereas 3)-4) are nanosize-specific. We will now discuss the relevance of these ingredients to the thermodynamics of hydrogen sorption by our

Mg-Ti-H NPs, with an eye to the data collected in Figure 10 and special focus on the  $\text{Mg} + \text{H}_2 \leftrightarrow \text{MgH}_2$  reaction.

The Mg-Ti-H system is quite prolific of metastable Mg-Ti and Mg-Ti-H phases, a peculiarity that has stimulated several investigations in the search of novel hydrogen storage materials [27,29,19,40,41,22,25,42]. Non-equilibrium synthesis techniques such as co-sputtering [29], ball milling [41,22] and gas phase condensation of atomic vapour mixtures [27,19,25] must be adopted in order to enforce the alloying of the two mutually insoluble metallic elements. However, independently on the synthesis method and initial state one uses, the material tends to attain thermodynamic equilibrium by decomposing into  $\text{MgH}_2$  and  $\text{TiH}_2$  upon cycling at elevated temperature [43,44]. In the present case, phase separation into  $\text{MgH}_2$  and  $\epsilon\text{-TiH}_2$  takes place at the individual NPs level, while Mg-Ti NPs grown under pure He and not exposed to hydrogen are made of a metastable single-phase  $\text{Mg}(\text{Ti})$  solid solution [27]. The transformation from  $\text{Mg}(\text{Ti})$  into  $\text{MgH}_2 + \text{TiH}_2$  likely occurs via short-range interdiffusion of Mg and Ti, driven by their mutual insolubility and by their different bonding strength to hydrogen. Once formed, the highly stable  $\text{TiH}_2$  phase ( $\Delta H = 125 \text{ kJ/molH}_2$ ,  $P_{\text{eq}} \approx 10^{-2} \text{ mbar}$  at  $300^\circ\text{C}$  [45]) remains unaltered under the pressure/temperature conditions applied in our experiments, as shown by XRD after hydrogen desorption (see Figure S7). *In situ* XRD carried out with synchrotron radiation on similar samples demonstrate that Mg is solely transformed into  $\text{MgH}_2$  (and vice versa) upon hydrogen absorption (desorption) [16]. Therefore, the dispersion of  $\text{TiH}_2$  within the NPs does not convey any new reactants/products capable of modifying the  $\text{Mg} + \text{H}_2 \leftrightarrow \text{MgH}_2$  thermodynamics. This conclusion, arising from the metastability of all Mg-Ti phases and from the high stability of  $\text{TiH}_2$ , was also drawn in the case of  $\text{MgH}_2\text{-TiH}_2$  ball-milled nanocomposites [14,13]. Differently, Anastasopol et al [19] have reported quite low enthalpy/entropy values in Mg-Ti-H NPs (data labelled “e” in Figure 10). There are several reasons for this discrepancy: the first is that, according to their XRD data (Figure 1 of ref. [19]), hydrogen absorption induces a transformation from a  $\text{Mg}_{0.5}\text{Ti}_{0.5}$  phase to a  $\text{Mg}_{0.5}\text{Ti}_{0.5}\text{H}$  phase. The second is that the data in ref. [19] only refer to absorption isotherms. The authors admit that, due to sluggish kinetics, desorption isotherms close to equilibrium at the lower temperature were not measurable, thus raising serious concerns about the correct determination of equilibrium properties. Finally, the NPs studied in ref. [19] were heavily oxidized (MgO being the overwhelming phase): this structural feature explains their poor kinetics and may seriously affect the determination of equilibrium properties because of hysteresis.

It is instructive to confront Mg-Ti-H NPs with the case of Mg-Pd-H NPs, in which various  $\text{Mg}_x\text{Pd}_y$  intermetallic compounds act as reactants during hydrogen absorption, producing  $\text{MgH}_2$  along with Pd-rich compounds [46,47], the reverse occurring on desorption. Again different is the case of Mg-Ni NPs, where thermodynamic changes are brought about by the  $\text{Mg}_2\text{Ni}$  phase, which reversibly transforms into the complex hydride  $\text{Mg}_2\text{NiH}_4$  with  $\Delta H$  and  $P_{\text{eq}}$  different from pure Mg [48].

The very low solubility of Ti in Mg and  $\text{MgH}_2$  (below 1 at.% according to XRD) also rules out the occurrence of significant  $\Delta H$  or  $\Delta S$  changes induced by alloying effects. In fact, even though theoretical calculations indicate that transition metal doping may locally weaken the Mg-H bonds around the dopant [37], a measurable global effect requires doping levels well above 1 at.%. Gremaud et al [49] determined the enthalpy of hydride formation in  $\text{Mg}_y\text{Ti}_{1-y}$  hydride thin films by combinatorial optical methods, demonstrating small changes (within  $\pm 3 \text{ kJ/molH}_2$ ) in the  $0.65 < y < 1$  range.

We therefore turn to nanosize-specific ingredients: the thermodynamic change  $\delta(\Delta G)$  induced by interface/surface free energy can be described by the following equation for the free energy of hydride formation [7,32]:

$$\delta(\Delta G) = \delta(\Delta H) - T\delta(\Delta S) \equiv \Delta G - \Delta G_{\text{bulk}} = \frac{\bar{V}_{\text{Mg}}}{V_{\text{Mg}}^{\text{NP}}} \sum_i (\{A\gamma\}_{\text{MgH}_2|i} - \{A\gamma\}_{\text{Mg}|i}) \quad (2)$$

where  $\bar{V}_{\text{Mg}}$  is the molar volume of Mg,  $V_{\text{Mg}}^{\text{NP}}$  is the volume occupied by Mg within a NP, and A and  $\gamma$  represent the interface area and the free energy per unit area, respectively. The subscripts ‘ $\text{MgH}_2|i$ ’ and ‘ $\text{Mg}|i$ ’ denote the  $i$ -th interface between  $\text{MgH}_2$  or Mg in the NP, and a surrounding phase. Each term in the summation

therefore represents the free energy change of a specific interface  $i$ , surfaces being included as solid-vacuum interfaces. In writing Eq. (2), we have assumed that phases other than Mg and MgH<sub>2</sub> do not react with hydrogen at the conditions of interest. The surface contribution to eq. (2) in the case of Mg was calculated at T=0 K (yielding the enthalpy change  $\delta(\Delta H)$ ) as a function of the particle size by different authors, and somewhat contradictory results were reported [36,6,50]. On one side, all calculations agree that  $\{\gamma\}_{\text{MgH}_2|\text{vacuum}} - \{\gamma\}_{\text{Mg}|\text{vacuum}} \equiv \Delta\gamma_{(\text{vac})} > 0$ . Shevlin et al calculated  $\Delta\gamma_{(\text{vac})} \approx 0.11 \text{ J/m}^2$  for MgH<sub>2</sub> (110) and Mg (0001) surfaces [36]. Therefore, according to eq. (2), the surface free energy should increasingly destabilize the hydride with decreasing  $V_{\text{NP}}$ , if the atomic-level structure did not change. However, for very small MgH<sub>2</sub> clusters containing less than 10 Mg atoms, recent calculations [36] indicate that a stabilizing reconstruction occurs, eventually leading to higher stability and dehydrogenation enthalpy compared to bulk MgH<sub>2</sub>. For NPs containing more than 20 Mg atoms (volume  $\sim 600 \text{ \AA}^3$ ) there is general consensus that rather small changes can be expected: for instance,  $\delta(\Delta H) \lesssim 2 \text{ kJ/molH}_2$  for NPs diameter larger than 5 nm [51]. At the typical size of our Mg-Ti-H NPs, all surface free energy calculations predict that  $\delta(\Delta H) \lesssim 1 \text{ kJ/molH}_2$ . The same applies to nanomaterials labelled *d-g* and *h* in Figure 10, while for the very small NPs labelled *c* (ref. [17]), one can estimate  $\delta(\Delta H) \approx 5 \text{ kJ/molH}_2$  assuming an average NPs diameter of 2 nm. In summary, surface free energy effects explain only partially the reduced dehydrogenation enthalpies reported in Figure 10.

More relevant thermodynamic changes require a high density of interfaces with a large specific free energy change  $\Delta\gamma$ . For the  $\text{Mg}|\text{TiH}_2 \rightarrow \text{MgH}_2|\text{TiH}_2$  interface transformation, optical transmission isotherms [7] measured  $\Delta\gamma_{(\text{TiH}_2)} \approx 0.33 \text{ J/m}^2$ , with dominant enthalpic character. Thanks to this relatively high value and by careful interface engineering, a clear destabilization was observed in ultra-thin MgH<sub>2</sub> layers sandwiched between TiH<sub>2</sub> (symbol labelled *i* in Figure 10) as well as in ultra-fine MgH<sub>2</sub> particles embedded within a TiH<sub>2</sub> matrix [21]. It must be remarked that a true destabilization can only be claimed if  $P_{\text{des}}$  rises above the bulk value [52]. For our NPs, the MgH<sub>2</sub>|TiH<sub>2</sub> interface area per unit volume of Mg can be estimated from the relative volume fractions and crystallite size  $d_{\text{TiH}_2}$  obtained by XRD. The resulting enthalpy change is:

$$\delta(\Delta H) = \frac{\bar{V}_{\text{Mg}} A_{\text{Mg}|\text{TiH}_2}}{V_{\text{Mg}}^{\text{NP}}} \Delta\gamma_{(\text{TiH}_2)} = \frac{6}{d_{\text{TiH}_2}} \frac{\bar{V}_{\text{Mg}} V_{\text{TiH}_2}}{V_{\text{Mg}}} \Delta\gamma_{(\text{TiH}_2)} \quad (4)$$

where we have assumed that TiH<sub>2</sub> does not change volume and shape upon hydrogen sorption by Mg so that its interface area with Mg and MgH<sub>2</sub> stays the same. With this rather crude estimate we obtain specific interface areas that span from  $\sim 0.3 \text{ nm}^{-1}$  to  $\sim 0.6 \text{ nm}^{-1}$  when  $X_{\text{Ti}}$  increases from 6 to 30 at.%. Correspondingly,  $\delta(\Delta H)$  varies from  $\sim 1.5$  to  $\sim 3.0 \text{ kJ/molH}_2$ . This interface effect may therefore contribute to reduce  $\Delta H$  in our Mg-Ti NPs, although it does not account for whole reduction  $\delta(\Delta H) \approx 6 \text{ kJ/molH}_2$  observed with respect to the bulk. Similar considerations apply to ball-milled MgH<sub>2</sub>-0.1TiH<sub>2</sub> nanocomposites (*g* in Figure 10) and MgH<sub>2</sub> nanocrystallites embedded in a LiCl matrix (*b* in Figure 10), although the  $\Delta\gamma$  value (and sign) for a Mg/LiCl  $\rightarrow$  MgH<sub>2</sub>/LiCl interface transformation is not known.

The last ingredient that may modify the thermodynamics are clamping effects, which occur when the hydride forming phase encounters an elastic constraint to volume expansion, due e.g. to coherent interfaces with inert phases or to a surrounding solid shell [9]. We believe that this is not the case in our Mg-Ti-H NPs, which are relatively free to expand and contract. Differently, elastic clamping is at the origin of increased  $P_{\text{eq}}$  in constrained Mg/Ti/Pd NDs (line *h* in Figure 10 [32]). The absence of volume constraints is likely the reason for the remarkably small hysteresis of the Mg-Ti-H NPs. Values of  $P_{\text{abs}}/P_{\text{des}}$  between 2 and 3 (Figure 7) are well below those of clamped systems such as multi-layered Mg films and NDs, for which the onset of plastic deformation widens the hysteresis considerably [32,53].

A comment is due at this point on the issue of enthalpy-entropy compensation [6,13]: this apparent correlation was reported several times in chemical and biological systems even when there was no plausible physical reason for its existence [20]. In many cases, it is only due to the narrow temperature range explored. Indeed, in many of the experiments reported in Figure 10 the absolute temperature varies by only 10%. This

does not allow an independent evaluation of the two fit parameters: slope and intercept, which correspond to  $\Delta H$  and  $\Delta S$ . Moreover, in some cases, only absorption data are used, and the presence of a temperature-dependent hysteresis may lead to erroneous slope and intercept values. As shown above, for the systems listed in Figure 10, nanostructural features may account for a maximum  $\delta(\Delta H)$  of about 5 kJ/mol  $H_2$ . These arguments suggest that, when significantly larger enthalpy change for the  $Mg + H_2 \leftrightarrow MgH_2$  reaction were obtained without correspondingly large  $P_{eq}$  changes, the reported enthalpy-entropy compensation was actually a phantom phenomenon caused by the restricted temperature range [20].

Our data average absorption and desorption plateaus and extend to remarkably low temperatures for a Mg-based system, covering the range from 1.8 to 2.9 in  $1000/T$ . Although far from spanning the whole decade that would allow for a robust statistical analysis, this is close to the best one can do given the inaccessibility of both higher temperatures (where the nanostructure is destroyed) and lower temperatures (due to freezing kinetics and very low equilibrium pressures). At low temperature, the  $P_{eq}$  of as-prepared NPs lie slightly above the extrapolated bulk Mg, which is compatible with a small destabilization due to nanostructural features. The microstructural coarsening that accompanies high temperature cycling could suppress this effect, bringing  $P_{eq}$  closer to bulk Mg with a resulting reduction of slope and intercept. The obtained  $\Delta H$  and  $\Delta S$  may therefore be slightly underestimated (in absolute value), which in turn reinforces the idea that thermodynamic changes compared to bulk Mg are small. A reduced desorption entropy could originate with a non-negligible entropy of hydrogen in the nanostructured hydride. In fact, the entropy of the bulk solid phases changes very little upon hydrogen sorption and the reaction entropy essentially coincides with the entropy of the gas. A possible source of entropy increase in the nano-hydride may be found in the configurational and vibrational entropy of hydrogen atoms located in disordered non-lattice sites, i.e. mainly at interfaces and surfaces. For instance, the vibrational spectrum of hydrogen in palladium grain boundaries contains excess low frequency modes that increase the vibrational entropy [54]. A modelling of entropy changes induced by nanostructural features such as surfaces and interfaces would help in assessing whether the reduced entropies often reported by experiments are reasonable.

The most remarkable properties of our Mg-Ti-H NPs are for sure the impressively fast sorption kinetics, key to the successful characterization of low-temperature equilibrium. The only  $MgH_2 \rightarrow Mg$  desorption isotherms below 425 K we are aware of were measured in Pd-coated thin films. In the other cases, close-to-equilibrium kinetics were too slow and only desorption against high vacuum could be measured below 425 K. The peculiar feature of our Mg-Ti-H NPs is that they can reversibly absorb and desorb a large amount of hydrogen at about 420 K on a timescale of minutes in the mbar range. The desorption rate of 0.18 wt%  $H_2$ /min at  $p(H_2) \sim 1$  mbar shown in Figure 8 is faster than 0.10 wt%  $H_2$ /min obtained on a benchmark  $MgH_2$ - $TiH_2$  ball milled composite at the same temperature, but far from equilibrium [55]. We suggest that such outstanding kinetic behaviour originates from the combination of two features, i.e. the fine  $TiH_2$  dispersion and the small NPs size in the 10-30 nm range. Several authors have demonstrated that addition of  $TiH_2$  strongly accelerates Mg sorption kinetics [14,16,13,24], however the exact mechanism behind this improvement is not well understood.  $TiH_2$  may provide catalytic active sites for surface adsorption and dissociation of  $H_2$ . As for desorption, it has been proposed that multiple valence Ti sites act as the intermediate for electron transfers between  $H^-$  and  $Mg^{2+}$ , which makes the surface recombination of  $H_2$  on Ti-containing compounds much easier [24]. Furthermore, hydrogen diffusion is faster in  $TiH_2$  than in  $MgH_2$  and therefore the  $TiH_2$  nanocrystallites may provide high mobility paths for atomic hydrogen. The use of a hydrogen atmosphere for the NPs condensation helps in limiting surface contamination, and  $TiH_2$  crystallites act as grain refiners to avoid extensive coarsening during low-temperature cycling. We believe that the purity of the NPs and the sorption kinetics could be further improved by using oxygen filters on the gas feed lines and by scaling up the amount of NPs (here about 50 mg) to share the residual oxygen impurities among a larger amount of material.

The thermodynamics and extraordinary kinetics of our Mg-Ti-H NPs make them unique materials for tuneable hydrogen (or heat) release / storage at mbar pressures, in a temperature range where other kinetically usable hydrides have lower hydrogen density, lower heat capacity and higher costs. The relatively small hysteresis

would surely be an advantage for those applications, in which the system must transition from storage to release in response to tiny variations of control parameters.

## CONCLUSIONS

Hydrogen absorption and desorption by Mg-Ti-H NPs under close-to-equilibrium conditions was characterized over the 340-550 K temperature range. This remarkable achievement was possible thanks to a careful NPs growth strategy coupled with *in situ* hydrogen sorption measurements in the synthesis chamber. To the best of our knowledge, hydrogen desorption isotherms below 425 K in Mg-based systems were previously explored only using thin films coated by a Pd catalyst layer. Over the whole temperature range, equilibrium pressures are within a factor of two from those calculated using  $\Delta H$  and  $\Delta S$  of bulk Mg, suggesting that thermodynamic changes induced by nanostructural features are rather small. In fact, we estimated that the high specific interface area in the composite NPs, where small TiH<sub>2</sub> crystallites are dispersed in a Mg or MgH<sub>2</sub> matrix, may lead to a maximum enthalpy change  $\delta(\Delta H) \approx 3.0$  kJ/mol H<sub>2</sub>. Experimentally we determined  $\delta(\Delta H) \approx 6.0$  kJ/molH<sub>2</sub>: irreversible microstructure coarsening upon high temperature cycling may be the reason for this discrepancy, which is anyhow small compared to the reference value,  $\Delta H_{bulk} \approx 74$  kJ/mol H<sub>2</sub>. A critical comparison of several literature data on Mg-based NPs confirms that the equilibrium pressures, if correctly determined by averaging absorption and desorption data, are always very close to bulk Mg. The enthalpy-entropy correlation, sometimes claimed in the literature to explain  $\delta(\Delta H)$  significantly larger than 5 kJ/mol H<sub>2</sub> without correspondingly large equilibrium changes, is likely a phantom statistical phenomenon caused by a too narrow temperature range. The Mg-Ti-H NPs exhibited impressively fast hydrogen sorption kinetics in the low temperature regime, demonstrating a benchmark desorption rate of 0.18 wt% H<sub>2</sub>/min at T=423 K and  $p(\text{H}_2) \approx 1$  mbar, coupled with a low pressure hysteresis  $P_{abs}/P_{des} \approx 2$ . Thanks to their peculiar equilibrium and kinetic properties, these Mg-Ti-H NPs stand as unique materials for reversible hydrogen / storage at mild temperatures and pressures.

## ACKNOWLEDGEMENTS

This research was partly supported by the European COST Action MP1103 “Nanostructured Materials for Solid State Hydrogen Storage”.

## FIGURE CAPTIONS

Figure 1: Sketch of the sequence used to determine plateau pressures for hydrogen absorption and desorption. I) the sample is heated at the desired temperature under  $p(\text{H}_2) \gg P_{eq}$  in order to avoid desorption. II)  $p(\text{H}_2)$  is rapidly decreased below  $P_{eq}$  and the system is allowed to reach equilibrium; the steady-state value provides the measure of  $P_{des}$ . III)  $\text{H}_2$  is released under high vacuum conditions. IV) a check is carried out to verify that desorption is completed. V)  $p(\text{H}_2)$  is rapidly increased above  $P_{eq}$  and the system is allowed to equilibrate again; the steady state value provides a measure of  $P_{abs}$ . Steps II and V are repeated at least once to ensure that the steady state correspond to metal-hydride coexistence at equilibrium.

Figure 2: XRD patterns of as prepared NPs with different Ti content  $X_{\text{Ti}}$ . Open circles are experimental data while the calculated Rietveld best fit is represented by the solid line. The fit residual is shown below each pattern, and the coloured vertical bars mark the Bragg reflections of the main crystalline phases. For  $\gamma\text{-MgH}_2$ , only the first four peaks are marked because the other ones are too weak. The Bragg peaks of metallic Mg, the fraction of which is always below 3 wt%, are not indicated.

Figure 3: HAADF-STEM images at different magnifications of as prepared Mg-6Ti (a, c) and Mg-30Ti (b, d) NPs; frames e, f display the corresponding STEM-EDX line scans taken along the red lines in c, d.

Figure 4: Pressure variations measured during the first hydrogen desorption (bottom, blue) and the first hydrogen absorption (top, red) on sample Mg-15Ti at 375 K. These curves correspond respectively to the steps II and V sketched in Figure 1. The equilibrium values  $P_{abs}$  and  $P_{des}$  are indicated, as well as the pressure change that corresponds to 1 wt% change due to hydrogen sorption by the sample.

Figure 5: Full PCI measured on sample Mg-15Ti at 375 K. The values  $P_{abs}$  and  $P_{des}$  derived from the curves reported in Figure 4 are indicated. The dotted lines are just a guide to the eye.

Figure 6: van 't Hoff plot of equilibrium pressures  $P_{eq}$  (log scale) versus  $T$  (reciprocal scale) measured on NPs samples with Ti content  $X_{\text{Ti}}=6, 15$ , and  $30$  at.%. The dashed red line is the best linear fit on NPs data only, from which the reported enthalpy-entropy values were obtained. The solid black line is an extrapolation of high temperature data on bulk Mg/MgH<sub>2</sub> [15].

Figure 7: Collection of pressure hysteresis values  $P_{abs} / P_{des}$  versus temperature measured on NPs samples with Ti content  $X_{\text{Ti}}=6, 15$ , and  $30$  at.%. The plot reports also values recently measured on Mg/Ti/Pd three-layer nanodots (NDs) with lateral size of 60 and 320 nm [32] and on a quasi-free Mg film 50 nm thick [7].

Figure 8: hydrogen absorption (bottom) and desorption (top) in sample Mg-15Ti at 423 K, starting from initial pressures far from the plateau values. The sorption rates obtained by a linear fit of the initial data (dashed lines) are indicated.

Figure 9: (a, b) HAADF-STEM images of Mg-15Ti NPs subjected to hydrogen sorption measurements at  $T < 425$  K; c and d represent the STEM-EDX line scans taken along the red lines in a and b, respectively.

Figure 10: compilation of van 't Hoff plots calculated from  $\Delta H$  and  $\Delta S$  data for Mg (b-d) and Mg-Ti (e-g) nanomaterials, confronted to bulk Mg (a, [56]) and to this work's results. Continuous lines represent  $P_{eq}$  values, while dotted lines with symbols depict  $P_{abs}$  values. The black dash-dotted line is the low temperature extrapolation of bulk Mg data. In the legend, the numbers in the columns denote the corresponding absolute values of  $\Delta H$  (left, in kJ/molH<sub>2</sub>) and  $\Delta S$  (right, in J/KmolH<sub>2</sub>). b: 2-7 nm Mg nanocrystallites in LiCl matrix [15]; c: < 3 nm Mg NPs in carbon scaffold [17]; d: 15 nm Mg NPs by electroless reduction [18]; e: 10-20 nm Mg-Ti NPs by spark discharge [19]; f: MgH<sub>2</sub>-TiH<sub>2</sub> nanocomposite (30 at.% Ti) [14]; g: MgH<sub>2</sub>-0.1TiH<sub>2</sub> nanocomposite [13]; h: Mg/Ti/Pd nanodots on silica, diameter 60 nm [32]; i: ultra-thin (2 nm) Mg film sandwiched between TiH<sub>2</sub> layers [7].

## REFERENCES

- [1] E. Callini, K.-F. Aguey-Zinsou, R. Ahuja, J. R. Ares, S. Bals, N. Biliškov, S. Chakraborty, G. Charalambopoulou, A.-L. Chaudhary, F. Cuevas, B. Dam, P. de Jongh, M. Dornheim, Y. Filinchuk, J. Grbović Novaković, M. Hirscher, T. R. Jensen, P. B. Jensen, N. Novaković, Q. Lai, F. Leardini, D. M. Gattia, L. Pasquini, T. Steriotis, S. Turner, T. Vegge, A. Züttel, and A. Montone, *Int. J. Hydrogen Energy* **41**, 14404 (2016).
- [2] A. Pundt and R. Kirchheim, *Annu. Rev. Mater. Res.* **36**, 555 (2006).
- [3] A. Borgschulte, R. Gremaud, and R. Griessen, *Phys. Rev. B - Condens. Matter Mater. Phys.* **78**, 1 (2008).
- [4] R. Griessen and Driessen, *Phys. Rev. B* **30**, 4372 (1984).
- [5] V. Berube, G. Chen, and M. S. Dresselhaus, *Int. J. Hydrogen Energy* **33**, 4122 (2008).
- [6] K. C. Kim, B. Dai, J. Karl Johnson, and D. S. Sholl, *Nanotechnology* **20**, 204001 (2009).
- [7] L. P. A. Mooij, A. Baldi, C. Boelsma, K. Shen, M. Wagemaker, Y. Pivak, H. Schreuders, R. Griessen, and B. Dam, *Adv. Energy Mater.* **1**, 754 (2011).
- [8] A. Baldi, M. Gonzalez-Silveira, V. Palmisano, B. Dam, and R. Griessen, *Phys. Rev. Lett.* **102**, 1 (2009).
- [9] L. Pasquini, M. Sacchi, M. Brighi, C. Boelsma, S. Bals, T. Perkisas, and B. Dam, *Int. J. Hydrogen Energy* **39**, (2014).
- [10] I. P. Jain, C. Lal, and A. Jain, *Int. J. Hydrogen Energy* **35**, 5133 (2010).
- [11] J. C. Crivello, B. Dam, R. V. Denys, M. Dornheim, D. M. Grant, J. Huot, T. R. Jensen, P. de Jongh, M. Latroche, C. Milanese, D. Milčius, G. S. Walker, C. J. Webb, C. Zlotea, and V. A. Yartys, *Appl. Phys. A Mater. Sci. Process.* **122**, (2016).
- [12] U. Bosenberg, D. B. Ravnsbæk, H. Hagemann, V. D'Anna, C. B. Minella, C. Pistidda, W. van Beek, T. R. Jensen, R. Bormann, and M. Dornheim, *J. Phys. Chem. C* **114**, 15212 (2010).
- [13] J. Lu, Y. J. Choi, Z. Z. Fang, H. Y. Sohn, and E. Rönnebro, *J. Am. Chem. Soc.* **131**, 15843 (2009).
- [14] F. Cuevas, D. Korablov, and M. Latroche, *Phys. Chem. Chem. Phys.* **14**, 1200 (2012).
- [15] M. Paskevicius, D. A. Sheppard, and C. E. Buckley, **6**, 469 (2010).
- [16] M. Calizzi, D. Chericoni, L. H. Jepsen, T. R. Jensen, and L. Pasquini, *Int. J. Hydrogen Energy* (2015).
- [17] Z. Zhao-Karger, J. Hu, A. Roth, D. Wang, C. Kübel, W. Lohstroh, and M. Fichtner, *Chem. Commun. (Camb)*. **46**, 8353 (2010).
- [18] W. Liu and K.-F. Aguey-Zinsou, *J. Mater. Chem. A* **2**, 9718 (2014).
- [19] A. Anastasopol, T. V. Pfeiffer, J. Middelkoop, U. Lafont, R. J. Canales-Perez, A. Schmidt-Ott, F. M. Mulder, and S. W. H. Eijt, *J. Am. Chem. Soc.* **135**, 7891 (2013).
- [20] A. Cornish-Bowden, *J. Biosci.* **27**, 121 (2002).
- [21] K. Asano, R. J. Westerwaal, A. Anastasopol, L. P. A. Mooij, C. Boelsma, P. Ngene, H. Schreuders, S. W. H. Eijt, and B. Dam, *J. Phys. Chem. C* **119**, 12157 (2015).
- [22] D. Korablov, F. Besenbacher, and T. R. Jensen, *Int. J. Hydrogen Energy* **39**, 9700 (2014).
- [23] M. Calizzi, F. Venturi, M. Ponthieu, F. Cuevas, V. Morandi, T. Perkisas, S. Bals, and L. Pasquini, *Phys. Chem. Chem. Phys.* **18**, 141 (2016).
- [24] J. Cui, H. Wang, J. Liu, L. Ouyang, Q. Zhang, D. Sun, X. Yao, and M. Zhu, *J. Mater. Chem. A* **1**, 5603 (2013).

- [25] G. Krishnan, R. F. Negrea, C. Ghica, G. H. ten Brink, B. J. Kooi, and G. Palasantzas, *Nanoscale* **6**, 11963 (2014).
- [26] S. X. Tao, P. H. L. Notten, R. A. Van Santen, and A. P. J. Jansen, *Phys. Rev. B - Condens. Matter Mater. Phys.* **83**, 1 (2011).
- [27] M. Calizzi, F. Venturi, M. Ponthieu, F. Cuevas, V. Morandi, T. Perkisas, S. Bals, and L. Pasquini, *Phys. Chem. Chem. Phys.* **18**, 141 (2016).
- [28] T. Noritake, M. Aoki, S. Towata, Y. Seno, Y. Hirose, E. Nishibori, M. Takata, and M. Sakata, *Appl. Phys. Lett.* **81**, 2008 (2002).
- [29] D. M. Borsa, R. Gremaud, A. Baldi, H. Schreuders, J. H. Rector, B. Kooi, P. Vermeulen, P. H. L. Notten, B. Dam, and R. Griessen, *Phys. Rev. B - Condens. Matter Mater. Phys.* **75**, 1 (2007).
- [30] P. E. Kalita, A. L. Cornelius, K. E. Lipinska-Kalita, C. L. Gobin, and H. Peter Liermann, *J. Phys. Chem. Solids* **69**, 2240 (2008).
- [31] L. Pasquini, E. Callini, E. Piscopiello, A. Montone, M. V. Antisari, and E. Bonetti, *Appl. Phys. Lett.* **94**, (2009).
- [32] A. Molinari, F. D'Amico, M. Calizzi, Y. Zheng, C. Boelsma, L. Mooij, Y. Lei, H. Hahn, B. Dam, and L. Pasquini, *Int. J. Hydrogen Energy* **41**, 9841 (2016).
- [33] L. Pasquini, A. Montone, E. Callini, M. V. Antisari, and E. Bonetti, *Appl. Phys. Lett.* **99**, (2011).
- [34] U. Boesenberg, S. Doppiu, L. Mosegaard, G. Barkhordarian, N. Eigen, A. Borgschulte, T. R. Jensen, Y. Cerenius, O. Gutfleisch, T. Klassen, M. Dornheim, and R. Bormann, *Acta Mater.* **55**, 3951 (2007).
- [35] C. P. Broedersz, R. Gremaud, B. Dam, R. Griessen, and O. M. Løvvik, *Phys. Rev. B - Condens. Matter Mater. Phys.* **77**, 1 (2008).
- [36] S. A. Shevlin and Z. X. Guo, *J. Phys. Chem. C* **117**, 10883 (2013).
- [37] B. Paskaš Mamula, J. Grbović Novaković, I. Radisavljević, N. Ivanović, and N. Novaković, *Int. J. Hydrogen Energy* **39**, 5874 (2014).
- [38] S. Q. Hao and D. S. Sholl, *J. Phys. Chem. C* **116**, 2045 (2012).
- [39] S. Wagner and A. Pundt, *Int. J. Hydrogen Energy* **41**, 2727 (2016).
- [40] P. Vermeulen, P. C. J. Graat, H. J. Wondergem, and P. H. L. Notten, *Int. J. Hydrogen Energy* **33**, 5646 (2008).
- [41] K. Asano, H. Enoki, and E. Akiba, *J. Alloys Compd.* **480**, 558 (2009).
- [42] S. Er, D. Tiwari, G. A. De Wijs, and G. Brocks, *Phys. Rev. B - Condens. Matter Mater. Phys.* **79**, 1 (2009).
- [43] G. Liang and R. Schulz, *J. Mater. Sci.* **38**, 1179 (2003).
- [44] S. Srinivasan, P. C. M. M. Magusin, W. P. Kalisvaart, P. H. L. Notten, F. Cuevas, M. Latroche, and R. A. van Santen, *Phys. Rev. B* **81**, 54107 (2010).
- [45] R. Wiswall, in *Hydrog. Met. II*, edited by G. Alefeld and J. Völkl (Springer-Verlag, Berlin Heidelberg New York, 1978), pp. 201–242.
- [46] L. Pasquini, F. Boscherini, E. Callini, C. Maurizio, L. Pasquali, M. Montecchi, and E. Bonetti, *Phys. Rev. B - Condens. Matter Mater. Phys.* **83**, (2011).
- [47] E. Callini, L. Pasquini, L. H. Rude, T. K. Nielsen, T. R. Jensen, and E. Bonetti, *J. Appl. Phys.* **108**, (2010).
- [48] E. Callini, L. Pasquini, T. R. Jensen, and E. Bonetti, *Int. J. Hydrogen Energy* **38**, (2013).



- [49] R. Gremaud, C. P. Broedersz, D. M. Borsa, A. Borgschulte, P. Mauron, H. Schreuders, J. H. Rector, B. Dam, and R. Griessen, *Adv. Mater.* **19**, 2813 (2007).
- [50] R. W. P. Wagemans, J. H. Van Lenthe, P. E. De Jongh, A. J. Van Dillen, and K. P. De Jong, *J. Am. Chem. Soc.* **127**, 16675 (2005).
- [51] D. S. Sholl, *Nanotechnology* **11** (2010).
- [52] R. Griessen, N. Strohhfeldt, and H. Giessen, *Nat. Mater.* **15**, 1 (2015).
- [53] Y. Pivak, H. Schreuders, and B. Dam, *Crystals* **2**, 710 (2012).
- [54] U. Stuhr, H. Wipf, K. Andersen, and H. Hahn, *Phys. Rev. Lett.* **81**, 1449 (1998).
- [55] Y. J. Choi, J. Lu, H. Y. Sohn, Z. Z. Fang, and E. Rönnebro, *J. Phys. Chem. C* **113**, 19344 (2009).
- [56] J. F. Stampfer, C. E. Holley, and J. F. Suttle, *J. Am. Chem. Soc.* **82**, 3504 (1960).

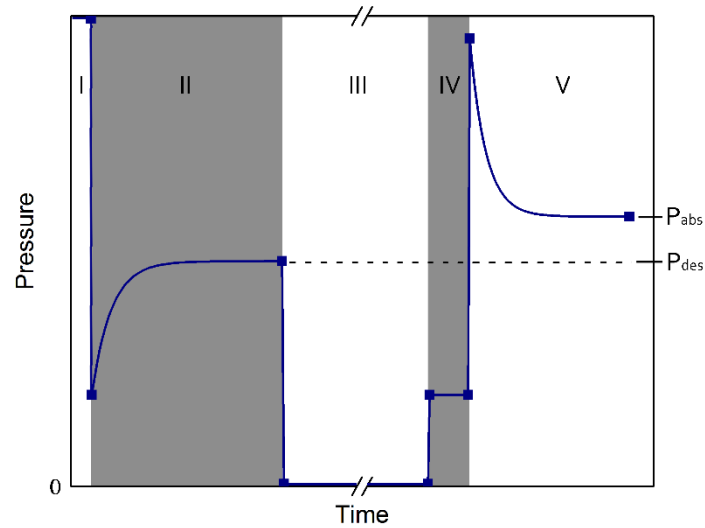


**Figure 1:** Sketch of the sequence used to determine plateau pressures for hydrogen absorption and desorption. I) the sample is heated at the desired temperature under  $p(\text{H}_2) \gg P_{eq}$  in order to avoid desorption. II)  $p(\text{H}_2)$  is rapidly decreased below  $P_{eq}$  and the system is allowed to reach equilibrium; the steady-state value provides the measure of  $P_{des}$ . III)  $\text{H}_2$  is released under high vacuum conditions. IV) a check is carried out to verify that desorption is completed. V)  $p(\text{H}_2)$  is rapidly increased above  $P_{eq}$  and the system is allowed to equilibrate again; the steady state value provides a measure of  $P_{abs}$ . Steps II and V are repeated at least once to ensure that the steady state correspond to metal-hydride coexistence at equilibrium.

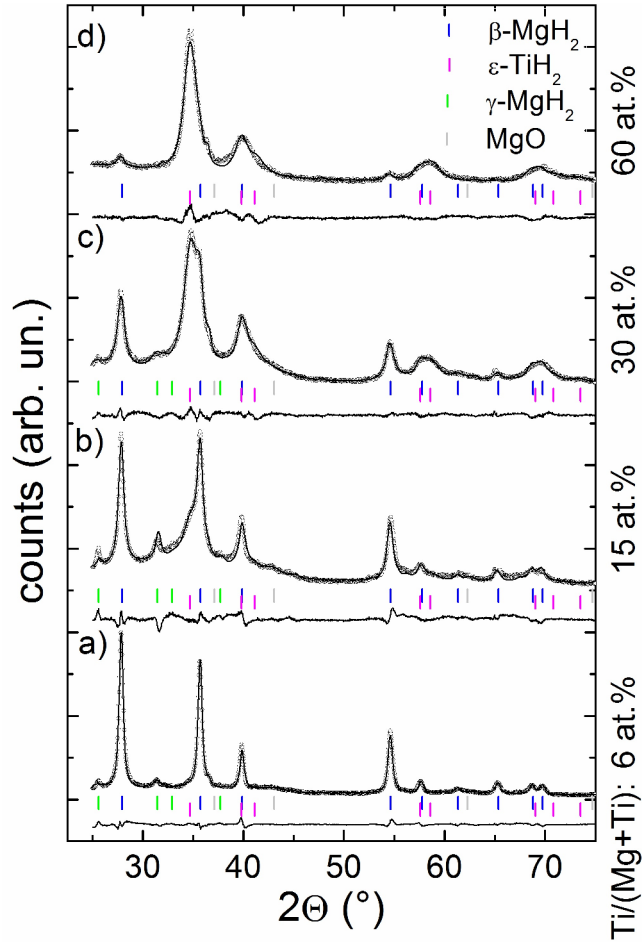


**Figure 2:** XRD patterns of as prepared NPs with different Ti content  $X_{\text{Ti}}$ . Open circles are experimental data while the calculated Rietveld best fit is represented by the solid line. The fit residual is shown below each pattern, and the coloured vertical bars mark the Bragg reflections of the main crystalline phases. For  $\gamma\text{-MgH}_2$ , only the first four peaks are marked because the other ones are too weak. The Bragg peaks of metallic Mg, the fraction of which is always below 3 wt%, are not indicated.

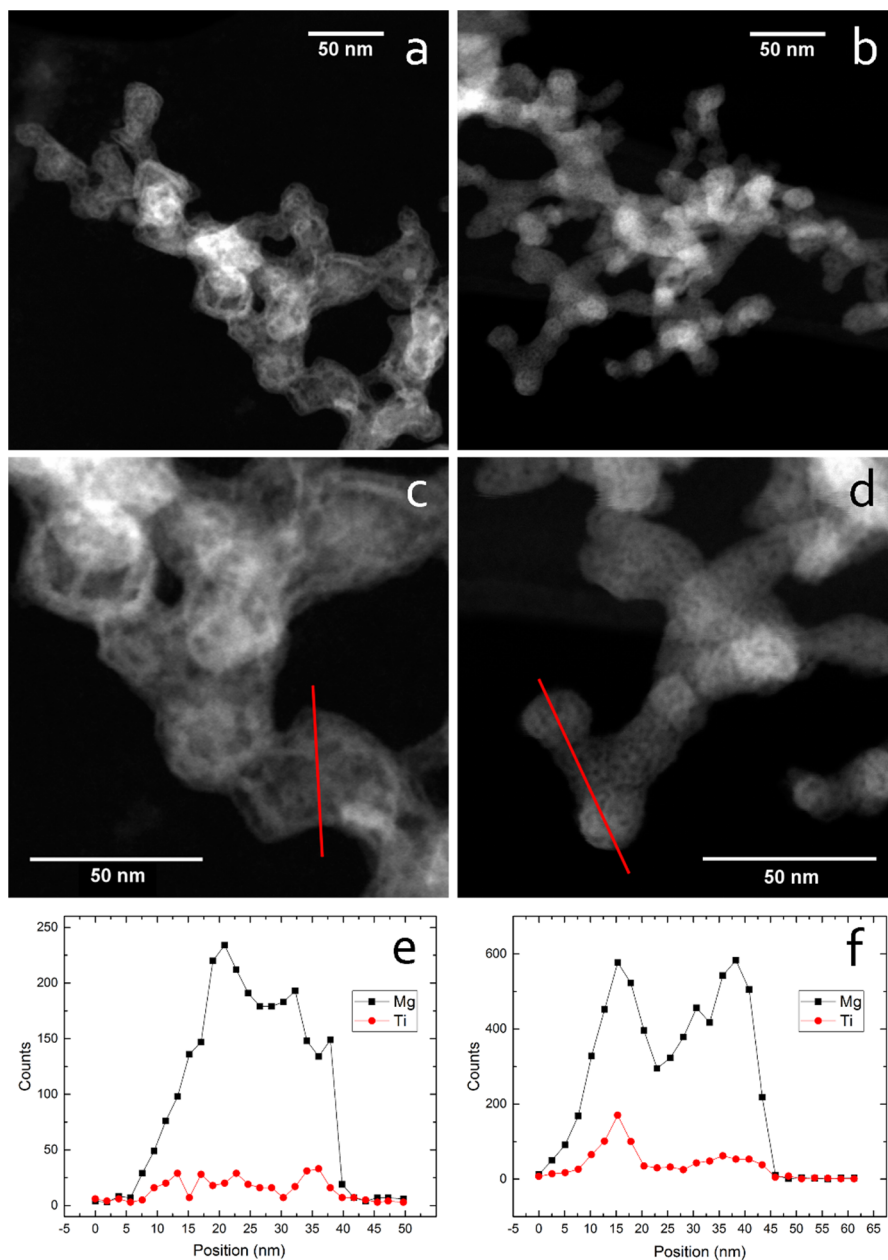


**Figure 3:** HAADF-STEM images at different magnifications of as prepared Mg-6Ti (a, c) and Mg-30Ti (b, d) NPs; frames e, f display the corresponding STEM-EDX line scans taken along the red lines in c, d.

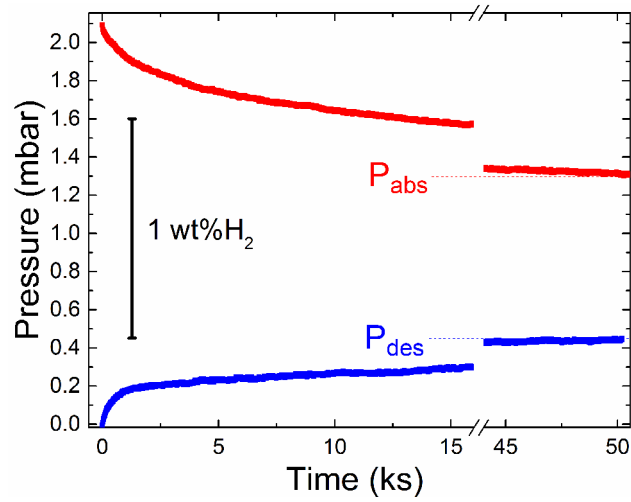


**Figure 4:** Pressure variations measured during the first hydrogen desorption (bottom, blue) and the first hydrogen absorption (top, red) on sample Mg-15Ti at 375 K. These curves correspond respectively to the steps II and V sketched in Figure 1. The equilibrium values  $P_{abs}$  and  $P_{des}$  are indicated, as well as the pressure change that corresponds to 1 wt% change due to hydrogen sorption by the sample.

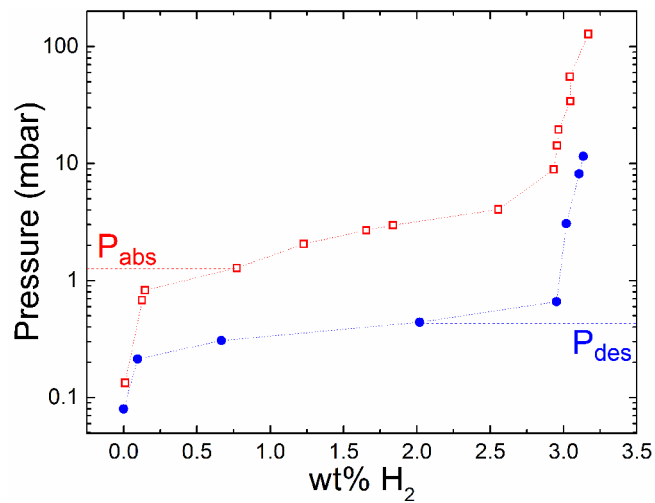


**Figure 5:** Full PCI measured on sample Mg-15Ti at 375 K. The values  $P_{abs}$  and  $P_{des}$  derived from the curves reported in Figure 4 are indicated. The dotted lines are just a guide to the eye.

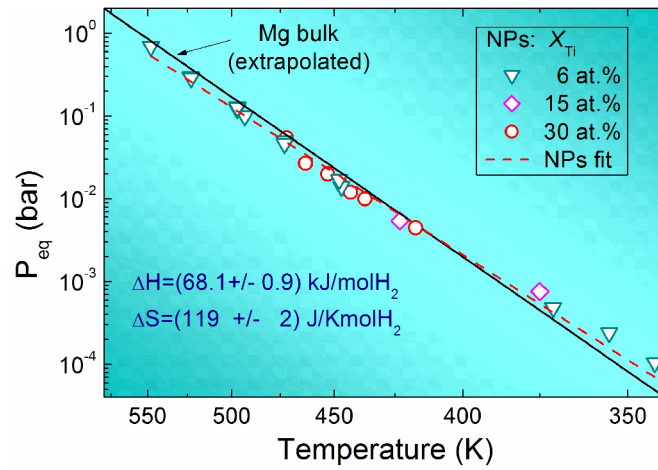


**Figure 6:** van 't Hoff plot of equilibrium pressures  $P_{eq}$  (log scale) versus T (reciprocal scale) measured on NPs samples with Ti content  $X_{Ti}$ =6, 15, and 30 at.%. The dashed red line is the best linear fit on NPs data, from which the reported  $\Delta H$  and  $\Delta S$  values were obtained. The solid black line was constructed using the  $\Delta H_{bulk}$  and  $\Delta S_{bulk}$  values (measured at higher temperatures).

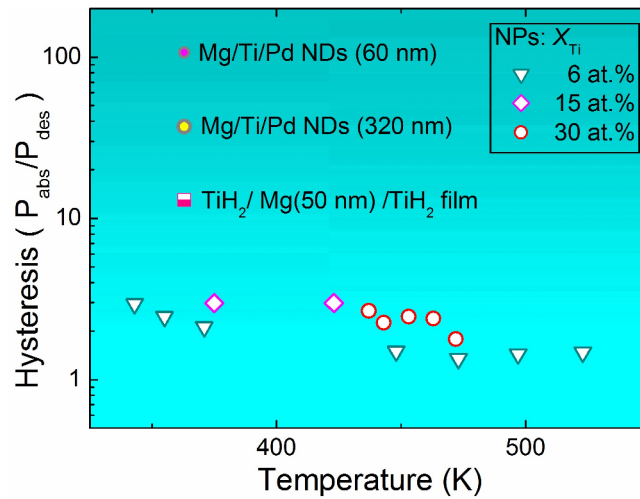


**FIGURE 7**

**Figure 7:** Collection of pressure hysteresis values  $P_{abs} / P_{des}$  versus temperature measured on NPs samples with Ti content  $X_{Ti}$ =6, 15, and 30 at.%. The plot reports also values recently measured on Mg/Ti/Pd three-layer nanodots (NDs) with lateral size of 60 and 320 nm [ref. Molinari] and on a quasi-free Mg film 50 nm thick [ref. Mooij]

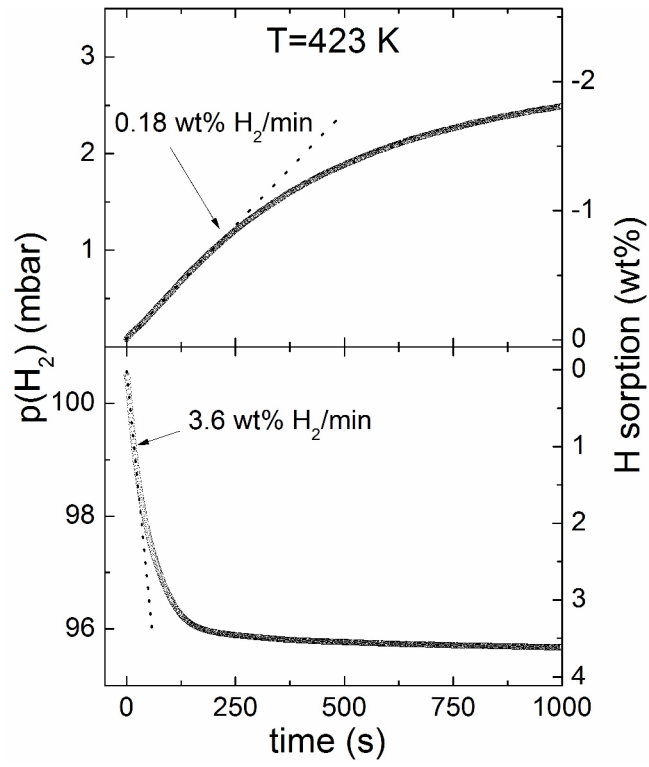


**Figure 8:** hydrogen absorption (bottom) and desorption (top) in sample Mg-15Ti at 423 K. The sorption rates obtained by a linear fit (dashed lines) of the initial data are indicated.

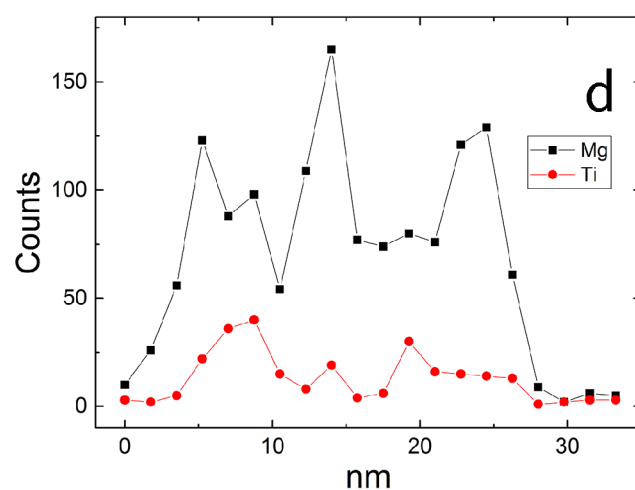
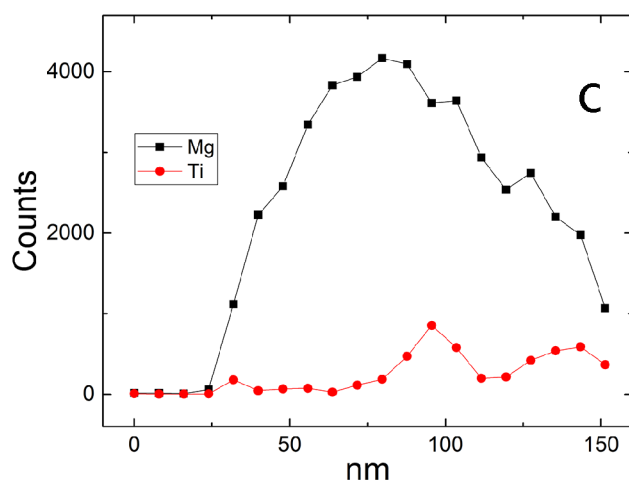
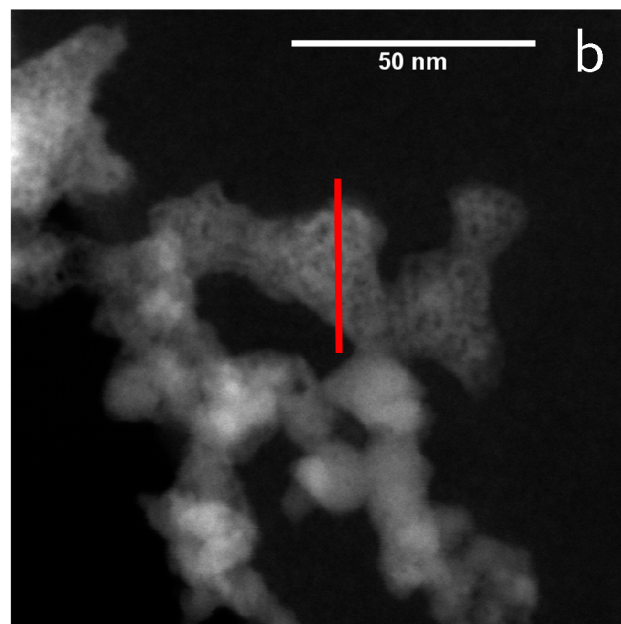
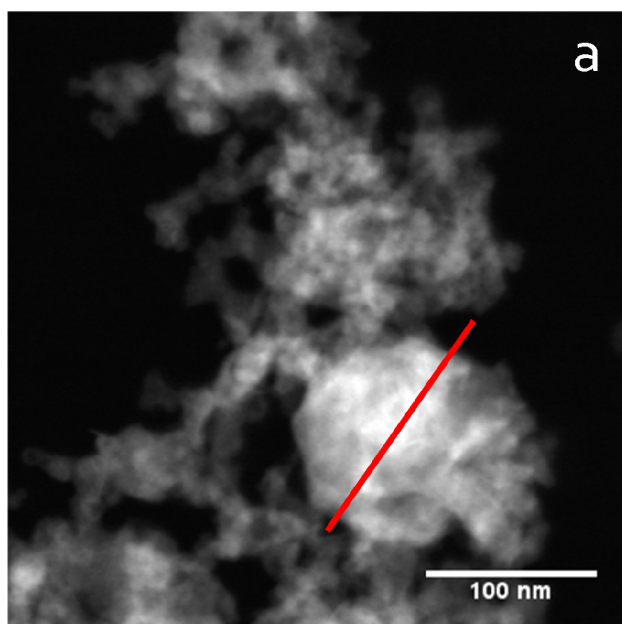


**Figure 9:** (a, b) HAADF-STEM images of Mg-15Ti NPs subjected to hydrogen sorption measurements at  $T < 425$  K; c and d represent the STEM-EDX line scans taken along the red lines in a and b, respectively.



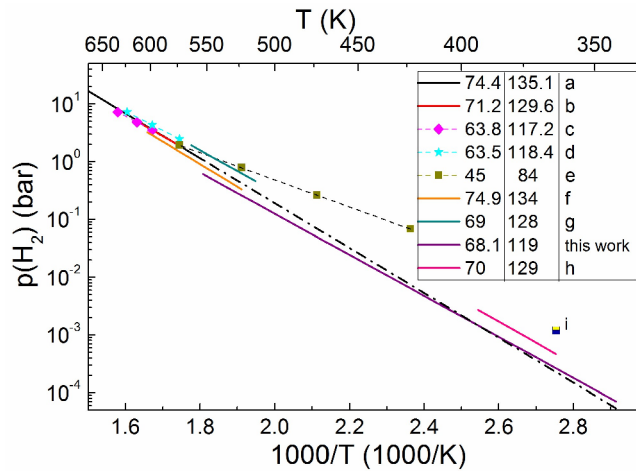


**Figure 10:** compilation of van 't Hoff plots calculated from  $\Delta H$  and  $\Delta S$  data for Mg (b-d) and Mg-Ti (e-g) nanomaterials, confronted to bulk Mg (a, [45]) and to this work's results. Continuous lines represent  $P_{eq}$  values, while dotted lines with symbols depict  $P_{abs}$  values. The black dash-dotted line is the low temperature extrapolation of bulk Mg data. In the legend, the numbers in the columns denote the corresponding absolute values of  $\Delta H$  (left, in kJ/molH<sub>2</sub>) and  $\Delta S$  (right, in J/KmolH<sub>2</sub>). b: 2-7 nm Mg nanocrystallites in LiCl matrix [7]; c: < 3 nm Mg NPs in carbon scaffold [39]; d: 15 nm Mg NPs by electroless reduction [11]; e: 10-20 nm Mg-Ti NPs by spark discharge [6]; f: MgH<sub>2</sub>-TiH<sub>2</sub> nanocomposite (30 at.% Ti) [1]; g: MgH<sub>2</sub>-0.1TiH<sub>2</sub> nanocomposite [32]; h: Mg/Ti/Pd nanodots on silica, diameter 60 nm [9]; i: ultra-thin (2 nm) Mg film sandwiched between TiH<sub>2</sub> layers [8].